A02-13721

AIAA 2002-0290

Highly-Resolved Three-Dimensional Velocity Measurements via Dual-Plane Stereo Particle Image Velocimetry (DSPIV) in Turbulent Flows

John A. Mullin and Werner J.A. Dahm

Laboratory for Turbulence & Combustion (LTC)
Department of Aerospace Engineering
The University of Michigan
Ann Arbor, MI 48109-2140

Highly-Resolved Three-Dimensional Velocity Measurements via Dual-Plane Stereo Particle Image Velocimetry (DSPIV) in Turbulent Flows

John A. Mullin[1] and Werner J.A. Dahm[2]

Laboratory for Turbulence & Combustion (LTC)
Department of Aerospace Engineering
The University of Michigan
Ann Arbor, MI 48109-2140

A frequency-based dual-plane stereoscopic particle image velocimetry (DSPIV) technique is presented that permits fully-resolved simultaneous measurement of all nine components of the instantaneous velocity gradient tensor field $\nabla\mathbf{u}(\mathbf{x},t)$ at the small scales of a turbulent flow. The technique is based on two essentially independent stereo PIV systems that provide three-component velocity measurements in two differentially-spaced light sheets of different colors, in this case 532 nm and 635 nm. Differentiation of the resulting velocity components within each plane and between the two planes yields all nine velocity gradient tensor $\partial u_i/\partial x_j$. Spatial scales relevant to the flow and the spatial resolution achievable with such measurements are discussed. Control of the light sheet thickness, separation, and parallelism over the field-of-view of the PIV cameras are essential for the technique. Methods to accurately measure and quantify these issues are presented, along with results for the present DSPIV configuration. A calibration method, error analysis, and system performance study using synthetic PIV data characterizes the accuracy of the DSPIV technique. Preliminary results show encouraging velocity vector fields in the two differentially-spaced data planes. The resulting velocity gradient field $\nabla\mathbf{u}(\mathbf{x},t)$ provides all three components of the vorticity vector field $\boldsymbol{\omega}(\mathbf{x},t)$ and all six components of the strain rate tensor field $\boldsymbol{\varepsilon}(\mathbf{x},t)$. These in turn permit access to fields of central relevance to the turbulence dynamics, including the kinetic energy dissipation rate field $2\nu\,\boldsymbol{\varepsilon}:\boldsymbol{\varepsilon}(\mathbf{x},t)$, the enstrophy field $\boldsymbol{\omega}:\boldsymbol{\omega}(\mathbf{x},t)$, and the enstrophy production rate field $\boldsymbol{\omega}\cdot\boldsymbol{\varepsilon}\cdot\boldsymbol{\omega}(\mathbf{x},t)$.

1. Introduction

The present study seeks to make fully-resolved measurements of the full nine-component velocity gradient tensor field at the small scales of a nonreacting turbulent shear flow, using a new two-color dual-plane stereo particle image velocimetry (DSPIV) technique. Such measurements will provide previously inaccessible experimental information on the structure and dynamics of the intermediate and small scales of turbulent shear flows, at conditions significantly exceeding those that can be addressed by direct numerical simulations (DNS). Data of this type are directly relevant to development of improved subgrid scale models for large eddy simulations (LES). In addition, such data can later be compared with analogous measurements from exothermic reacting turbulent flows to provide insights into subgrid scale modeling of reaction heat release effects on the intermediate and small scales of the flow.

Multi-dimensional velocity field measurements in turbulent flows have principally been based on particle imaging methods. The most common of these typically provide access to two components of the velocity field in a single imaging plane. Recently, however, such techniques have been extended to provide three-component velocity measurements in a single plane, and in some cases in multiple planes. Most of these techniques are also based on particle imaging, and apply auto- or cross-correlation techniques to the resulting particle images to obtain velocity fields. Stereoscopic particle image velocimetry (SPIV) uses two cameras in a stereo imaging arrangement to resolve the out-of-plane component of velocity while also measuring the in-plane components of velocity. Willert (1997) used this arrangement to investigate the unsteady velocity field of a vortex passing through a laser light sheet. Virant & Dracos (1997) used 3D particle tracking velocimetry (PTV) to measure the velocity field in a finite volume illuminated by a thick laser sheet in an open channel flow. Three-dimensional scanning PIV consists of scanning a laser light sheet through a volume and then using spatial cross-correlations of the overlapping sheets to reproduce the three-dimensional velocity field. Bruckner (1997) used this method to investigate the velocity field in a motored model engine. Holographic particle image velocimetry (HPIV) provides yet another volumetric technique, in which holographic images of particles in the flow are used to create the three-dimensional velocity field throughout a volume. Meng (1999) used this technique in an acoustically excited air jet and in the wake of a surface-mounted tab in a water channel flow. Raffel *et al*

---

[1] AIAA Student Member; Corresponding author.

[2] Professor of Aerospace Engineering; Head, Laboratory for Turbulence & Combustion (LTC); AIAA Associate Fellow.

(1995) used dual-plane particle image velocimetry to obtain all three components of the velocity in a single plane for the flow produced by a vortex. They used two closely-spaced planes of standard PIV data to extract the third (out-of-plane) component of velocity using correlation techniques. Kahler & Kompenhans (1999) used a similar approach by combining two closely-spaced planes of stereoscopic particle image velocimetry (SPIV) in their dual-plane stereo PIV measurements.

The dual-plane stereoscopic particle image velocimetry (DSPIV) technique used in the present study is somewhat similar to that of Kahler & Kompenhans (1999). Here we investigate the ability of such a system to make high-resolution three-dimensional velocity measurements that allow accurate assessment of all nine-components of the velocity gradient tensor field in a turbulent flow. Although the present data are from a turbulent jet, we are interested in measurements at the local small scales of the flow. Therefore, allowing an understanding and application of the technique within the general framework of turbulent shear flows.

2. Dual-Plane Stereoscopic PIV (DSPIV)

Dual-plane stereoscopic PIV is based on two simultaneous independent stereo PIV measurements in two closely-spaced light sheets. The two SPIV measurements provide the u, v, and w velocity components in two differentially-separated planes, which can then be differentiated in the x, y, and z directions to yield all nine components of the velocity gradient tensor field $\nabla\mathbf{u}(\mathbf{x},t)$ in a single plane, as indicated in Fig. 1. (Note that certain second derivatives of the velocity field are accessible as well, though these are typically of less practical interest). The resulting $\nabla\mathbf{u}(\mathbf{x},t)$ data provide all three components of the vorticity vector field $\boldsymbol{\omega}(\mathbf{x},t)$ and all six components of the strain rate tensor field $\boldsymbol{\varepsilon}(\mathbf{x},t)$. These fields, in turn, permit access to a variety of fields of central relevance to the turbulence dynamics, including the kinetic energy dissipation rate field $2\nu\,\boldsymbol{\varepsilon}:\boldsymbol{\varepsilon}(\mathbf{x},t)$, the enstrophy field $\boldsymbol{\omega}:\boldsymbol{\omega}(\mathbf{x},t)$, and the enstrophy production rate field $\boldsymbol{\omega}\cdot\boldsymbol{\varepsilon}\cdot\boldsymbol{\omega}(\mathbf{x},t)$.

A central issue in such DSPIV measurements involves separating the scattering signal from the two respective light sheets. This separation can be accomplished by using either different polarizations or different frequencies in the two light sheets. The former approach uses two orthogonally-polarized laser light sheets in conjunction with the respective optics to separate the polarized scattering signal onto the respective PIV camera pairs. Such an approach was used by Kahler & Kompenhans (1999) and by Hu *el al* (2000). Polarization optics are used to combine and maintain the polarization of the beams over the light path, and polarizing beam-splitting cubes are necessary to separate the scattering signal in front of the cameras.

The frequency-based approach uses two different wavelengths for the two light sheets in conjunction with narrow-band optical filters to separate the scattered light onto the respective PIV camera pairs. It is this approach that will be examined here. In principle, such a frequency-based approach could permit planar laser induced fluorescence (PLIF) measurements of molecular species concentrations in conjunction with simultaneous DSPIV measurements of the underlying strain rate and vorticity fields, as might be of interest in turbulent reacting flow applications. In that case, one of the two frequencies in the DSPIV measurement would be tuned to a fluorecence transition for the species of interest. The use a dye laser to shift the light frequency in combination with broadband optics and optical filters for the cameras would provide for a relatively simple illumination scheme to permit such simultaneous measurements.

3. Frequency-Based DSPIV Technique

The DSPIV system assembled for this study consists of two essentially independent stereoscopic particle image velocimetry systems that simultaneously provide measurements in two differentially spaced data planes. Each of these is a single-color double-frame/double-exposure planar PIV system, one of which operates with a coincident pair of 532 nm light sheets and the other with 635 nm laser light sheets. In the current system configuration, shown in Fig. 2, the two pairs of stereo PIV cameras are arranged in a forward-forward scattering configuration. This allows the scattering light intensity at both frequencies to be maximized, since the scatteried intensity is approximately an order of magnitude higher in forward scattering than in backward scattering.

To illuminate the seed particles in the field-of-view, two pairs of light sheets are created using four frequency-doubled Nd:YAG lasers. Two of these are sequentially triggered to create the double pulses for the 532 nm sheets, separated by a time delay Δt. The other two are also sequentially triggered, at the same two instants of time, to produce 532 nm output that double-pumps a dye laser to provide the double pulses for the 635 nm sheet. The resulting pairs of green and red beams travel through a set a sheet forming optics that produce 800 μm thick light sheets in the measurement region. The out-of-plane spacing between the green and red light sheets was set to 400 μm.

Note that thinner light sheets and closer sheet spacings will not provide higher spatial resolution, since the effective resolution of

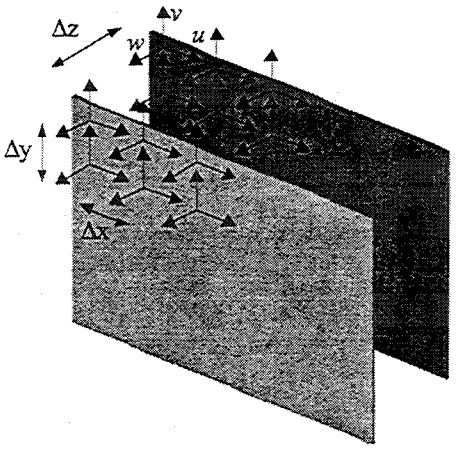

Figure 1. Basic arrangement for frequency-based dual-plane stereo PIV (DSPIV) measurements, showing simultaneous independent stereo PIV measurement of all three velocity components (u,v,w) in two differentially-spaced parallel green and red light sheets. The sheet thickness and spacing, as well as the final PIV correlation window size, are sufficiently small relative to the inner scale of the turbulent flow to permit differentiation within and between sheets to obtain all nine components of the velocity gradient tensor field $\nabla\mathbf{u}(\mathbf{x},t)$.

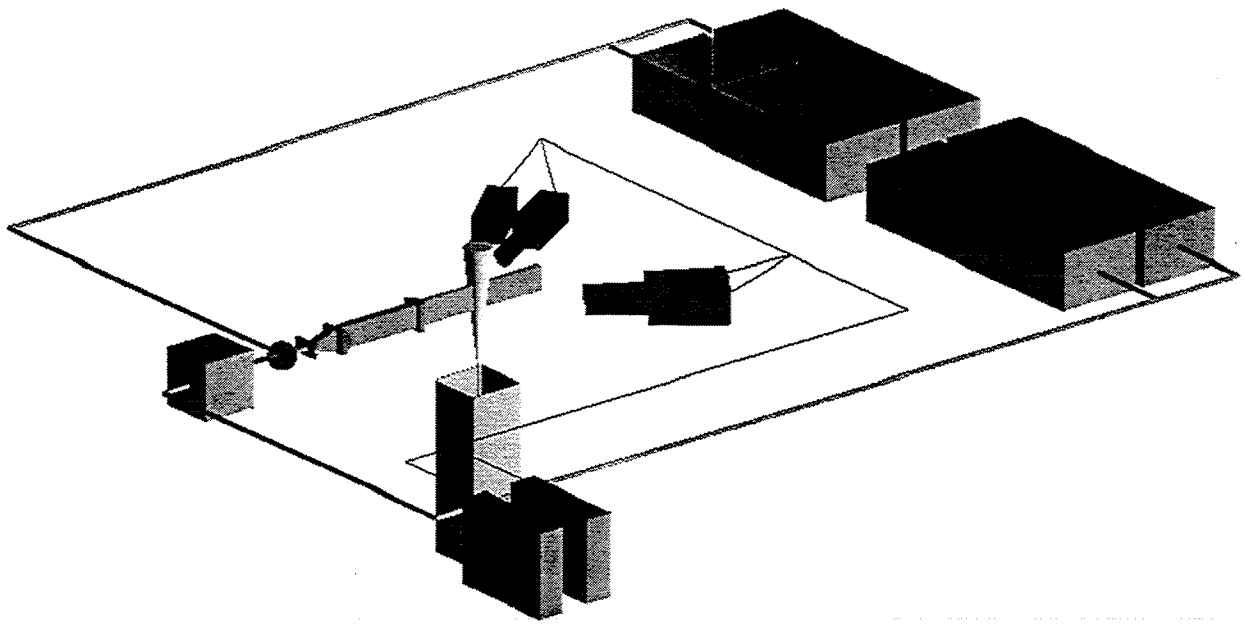

Figure 2. Dual-plane stereoscopic particle image velocimetry (DSPIV) system configured as two stereo PIV systems coupled to take simultaneous data in two differentially-spaced green (532nm) and red (635nm) laser sheets. The four Nd:YAG lasers provide two green sheets and (via a dye laser) two red sheets. Four 1280 × 1024 pixel PIV cameras with green and red interference filters are arranged in an asymmetric forward-forward scatter configuration so that each camera pair receives scattered light from one laser sheet. Macro lenses provide for a 15.5mm × 12.5 mm field-of-view that permits full resolution of the local scales of motion in the turbulent flow.

the measurements is instead dictated by the interrogation window size (Δx, Δy) used for the in-plane stereo PIV processing of each of the green and red particle image pairs. This interrogation window size is, in turn, set by Adrian's quarter-rule for the fraction of seed particles that can enter or leave the interrogation window between the two pulses. The window size implied by this rule is fixed by the somewhat larger axial (in-plane) velocity component of the turbulent jet flow, rather than by the azimuthal (out-of-plane) velocity component. The resulting 400 μm window size then dictated, ideally, a 400 μm light sheet thickness, for which the interrogation region in the stereo PIV processing thus becomes a cubic volume satisfying the quarter-rule. The out-of-plane separation Δz between the green and red sheets was then chosen to match this effective spatial resolution, as indicated Fig. 3. Based on these considerations, it is apparent that the spatial resolution of the resulting measurements is indirectly determined by the time delay Δt between each pair of laser pulses.

The flashlamps and Q-switches were triggered by 5V TTL signals at 10 Hz with a pulse duration of 10 nsec. The time delay Δt between pulses was controlled by a PC-based programmable timing unit (PTU) in a pair of master/slave computers running the LaVision Davis 6.2 PIV software package. All four lasers have an 100 nsec intrinsic delay between the rising edge of the trigger pulse and the actual peak of the laser energy; this additional delay is negligible for the flow conditions used in this study. In the present study, a pulse separation of $\Delta t \approx 80$ msec was found to provide the best system performance.

The particle images were recorded on four SensiCam PCO interline transfer CCD cameras with 200 nsec interframe timing. The 1280 × 1024 pixel array provides sufficiently high spatial dynamic range in the particle images, and 12-bit signal depth provides sufficient signal dynamic range. Each camera is equipped with a Sigma 70-300mm f/4-5.6 APO macro lens to allow the 1:1.8 imaging necessary to achieve the desired field-of-view for the measurements.

The four cameras are arranged in an angular displacement configuration, as shown in Fig. 4, with each of the green and red camera pairs satisfying the Scheimpflug condition for stereoscopic imaging (Prasad & Jensen 1995). Each pair of cameras is positioned to keep the included angle between the optical axis constant at 50-degrees. In the forward-forward configuration used here, this included angle consists of the two camera angles relative to the normal from the object plane. To accomplish this, one camera from each pair is arranged with a viewing angle of 20-degrees and the other with a viewing angle of 30-degrees, thus creating an asymmetric angular configuration for each camera pair. Coudert *et al* (1999) explored the performance of such asymmetric SPIV arrangements. Their results indicate that, for the present arrangement using a 50-degree included angle and a 10-degree asymmetry angle between camera pairs, the ratio of out-of-plane rms error to in-plane rms error is expected to be about 1-2 %. Note that this error ratio is similar to values obtained by Lawson & Wu (1997) for a symmetric SPIV arrangement, indicating that effects of the asymmetry in the camera ar-

rangement are essentially negligible.

Each pair of CCD cameras is equipped with narrow band filters centered at either 532 ± 5 nm or 632 ± 5 nm, depending on which laser sheet they are focused on. The filters isolate the respective scattered light from the laser sheet for the appropriate pair of cameras. For each camera, particle images from the first laser pulse are recorded onto the first frame and then immediately shifted under the submask. The particle images from the second laser pulse are then stored on the second frame after the time separation Δt. The camera and the laser pulse timing signals are generated by the PTU. In this double-frame/double-exposure PIV mode, each camera can acquire four particle image pairs per second.

The particle images are transferred to a master and slave computer (dual processor 500 MHz CPUs with 1 GB of RAM) for processing. The images are analyzed using a cross-correlation method with an FFT-based algorithm (Raffel *et al* 1998) using the Davis 6.2 commercial software package from LaVision. An adaptive multipass technique is used that calculates the velocity field on a coarse grid in the first pass, and refines this calculation on each subsequent pass using successively smaller interrogation window sizes, with the velocity field from the previous pass providing the initial estimate for the location of the correlation peak. This method allows the final interrogation window size to be much smaller than would be possible on a single pass, thereby increasing the effective spatial resolution. The present work uses an initial window size of 64 × 64 pixels, and the final pass is made with an interrogation window size of 32 × 32 pixels. This produces a final in-plane spatial resolution of 400 μm based on the magnification and physical pixel size. The velocity fields are then further processed to replace spurious vectors (< 10% of total vectors) via interpolation with a 3 × 3 median filter.

In a DSPIV measurement, a separate three-component velocity field is obtained in the two closely-spaced green and red light sheet planes. Differentiation of the resulting u-, v-, and w-component fields in the x- and y-directions within each plane, and in the z-direction between the two planes, then permits all nine components of the velocity gradient tensor field $\nabla\mathbf{u}(\mathbf{x},t)$ to be determined in one plane. Derivatives are obtained using standard central difference operators. Once the velocity gradient quantities are obtained then the dynamical quantities of interest can be computed. The accuracy and resolution of the resulting $\nabla\mathbf{u}(\mathbf{x},t)$ data are determined by a number of factors, each of which will be discussed below.

Particle Stokes Number

An implicit assumption in any PIV technique is the accuracy with which particle displacements are related to fluid displacements. Due to differences in the fluid and particle mass densities, the inertia of the particles must be overcome by the viscous drag induced on them by velocity gradients in the flow. These considerations lead to a classical particle Stokes number criterion that the flow and the seed particles must satisfy to essentially eliminate particle slip relative to the fluid. Denoting τ_p and τ_f, respectively, as the characteristic particle and flow time scales, then the particle Stokes number becomes

$$St \equiv \frac{\tau_p}{\tau_f} \quad . \tag{1}$$

From Stokes law for spherical particles, the particle relaxation time (for $Kn \ll 1$) is given by

$$\tau_p = \frac{\rho_p d_p^2}{18\mu} \quad . \tag{2}$$

In a shear flow such as the turbulent jet used in the present study, the fluid time scale can be expressed in the local outer-scale variables, namely the length scale δ and velocity scale u that characterize the local mean shear $\partial u/\partial r$. For the jet, these length and velocity scales are the local half-width of the jet and the mean centerline velocity, and thus

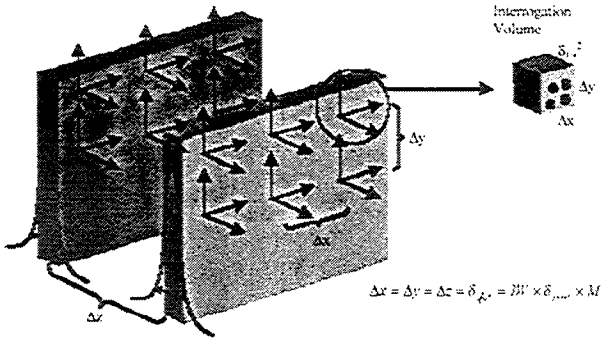

Figure 3. Schematic representation of green and red sheets, showing interrogation window size matched to laser sheet thickness. Reduction in laser sheet thickness does not provide for increase in spatial resolution. Note that actual separation between green and red sheets is 800 μm.

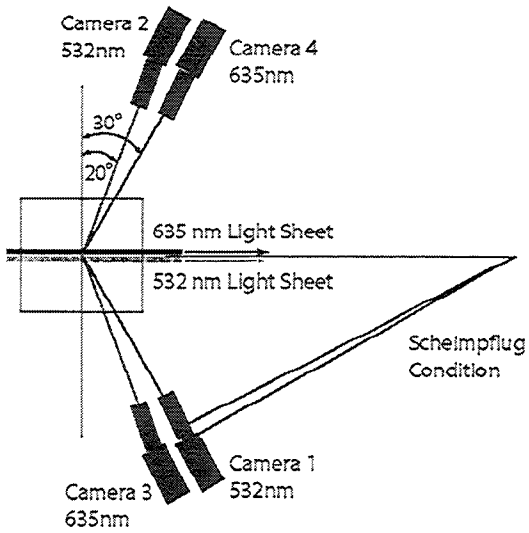

Figure 4. Asymmetric forward-forward scatter arrangement of the four PIV cameras, showing one camera in each color-pair oriented at 20-degrees and the other at 30-degrees relative to the sheet-normal.

$$\tau_f \approx \frac{\delta}{u} \quad . \tag{3}$$

With this definition of the flow time scale, Clemens & Mungal (1991) found the criterion for essentially negligible particle slip to be $St < 0.5$; note that this is in agreement with the results of Samimy & Lele (1991) from direct numerical simulations of particle slip for a different definition of the flow time scale.

While the particle diameter and density must be small enough to follow the flow, the particles must also be large enough to provide sufficient Mie scattering signal. Melling (1997) conducted a review of many seed particle types and their flow tracking capabilities and scattering characteristics. Aluminum oxide Al_2O_3 particles with a 0.5 μm diameter where chosen for this experiment, for which the particle relaxation time is obtained as 2.85 μs. For the flow conditions used in the present study, the characteristic flow time scale is 0.05 sec, giving the particle Stokes number as $St \approx 6\ (10^{-5})$. This readily meets the criterion noted above for the particles to follow the flow.

4. DSPIV Measurement Resolution Issues

Outer and Inner Scales

In shear-driven turbulent flows, the local outer length and velocity scales u and δ are those that characterize the local mean shear profile. All flow quantities associated with the outer scales are properly normalized by u and δ, and thus the local outer time scale is $\tau_\delta \equiv \delta/u$. The resulting local outer-scale Reynolds number $Re_\delta \equiv u\delta/\nu$ then properly scales the local turbulence properties of the flow, key among which is the relation between the local outer scales and the local inner scales.

The inner scales in turbulent flows characterize the finest length scale and Lagrangian time scale on which variations occur in the flow. The inner length scale results from the competing effects of strain, which acts to decrease the length scale over which gradients occur, and molecular diffusion, which acts to increase the gradient length scale. These two processes reach an equilibrium at the strain-limited viscous diffusion length scale λ_ν in the velocity gradient field, and at the strain-limited scalar diffusion length scale λ_D in the scalar gradient field. These inner length scales are related to the local outer scale δ as $\lambda_\nu \approx \Lambda\ \delta\ Re_\delta^{-3/4}$. The constant $\Lambda \approx 11.2$ comes from direct measurements of Buch & Dahm (1996*a,b*) and Southerland & Dahm (1996), with λ_ν defined from the layer-normal scalar dissipation profile as the distance between the points where the dissipation drops to 20% of the local profile maximum value. Note that, in terms of the local outer-scale Reynolds number Re_δ the value of Λ above should be universal. This has been confirmed by measurements of Su & Clemens (1998, 1999*a,b*), who obtained essentially the same value of Λ and verified the $Re_\delta^{-3/4}$ dependence of λ_ν.

The inner (viscous) length scale λ_ν is directly proportional to the classical Kolmogorov length scale $\lambda_K \equiv (\nu^3/\varepsilon)^{1/4}$ defined in terms of the mean dissipation rate ε. Using the dissipation results in turbulent jets of Friehe, van Atta & Gibson (1971) and Λ as above gives $\lambda_\nu \approx 5.9\ \lambda_K$. Note that although λ_K gives the correct parametric scaling for the finest velocity gradient length scale, it is defined entirely on dimensional grounds and thus does not correspond directly to the resolution requirement. Indeed, DNS studies have verified that the finest length scale in turbulent flows is larger than λ_K by about a factor of 6, as implied by the results above for the same definition of λ_ν. Note also that, in the same manner, the scalar diffusion length scale λ_D is proportional to the Batchelor scale, but gives the physical thickness of the scalar dissipation layers in a turbulent flow.

Apart from the inner length scale λ_ν, the viscosity is the only other directly relevant physical parameter at the inner scales, and thus the corresponding inner time scale is $\tau_\nu = (\lambda_\nu^2/\nu)$. This gives the shortest time scale on which the underlying vorticity field evolves in a Lagrangian frame. The local outer-scale Reynolds number Re_δ then provides the relation to the local outer time scale as $\tau_\nu \approx \Lambda^2\ \tau_\delta \cdot Re_\delta^{-1/2}$, where $\tau_\delta \equiv (\delta/u)$. The inner time scale is directly proportional to the classical Kolmogorov time scale $\tau_K \equiv (\nu/\varepsilon)^{1/2}$, where as above $\tau_K \approx 35\ \tau_\nu$.

When the outer scale Reynolds number Re_δ is sufficiently large, the velocity field $\mathbf{u}(\mathbf{x},t)$ should, when viewed on the inner scales, be essentially independent of Re_δ. Moreover, since the outer variables enter the governing equations only through Re_δ, the velocity field should therefore also be independent of the outer scale variables and, as a further consequence, be independent also of the particular shear flow as well. It is in this sense that the fine scale structure of the velocity fields, when viewed on the inner scales of high Reynolds number turbulent flows, are largely universal (*i.e.* independent of the Reynolds number and of the particular flow).

Eulerian (Advection) Scales

The inner Lagrangian time scale τ_ν is not, however, the temporal resolution requirement for turbulent flow measurements. The Eulerian nature of measurements obtained at any fixed spatial point introduces the much shorter viscous advection time scale $T_\nu \equiv (\lambda_\nu/u)$ in the velocity gradient field, and the corresponding scalar advection time scale $T_D \equiv (\lambda_D/u)$ in the scalar gradient field. Fully-resolved velocity or scalar field measurements thus need to meet these much more stringent Eulerian resolution requirements. Note that these can be related to the local inner time scale as $\tau_\nu = \Lambda\ T_\nu \cdot Re_\delta^{1/4}$, and to the local outer time scale as $\tau_\delta = (T_\nu/\Lambda) \cdot Re_\delta^{3/4}$.

Note that statistics of velocity and scalar fields obtained from time-series measurements will converge on the outer time scale (δ/u), while velocity gradient and scalar gradient statistics converge on the advective time scale T_ν or T_D for Eulerian time-series measurements, and on the inner length scale λ_ν or λ_D for spatial measurements.

Fully-Resolved Measurements

Full resolution of velocity field measurements in a turbulent flow thus requires sufficiently high resolution relative to λ_ν in space and relative to T_ν in time to permit determination of the velocity gradient tensor field $\nabla\mathbf{u}(\mathbf{x},t)$. In practice a "grid convergence" procedure, much as used in numerical simulations, can be used to assess if a given set of experimental data is "fully resolved". We will consider an arbitrary measured field quantity $f(\mathbf{x},t)$, and consider the integral (over the measurement domain) of the dissipation field $\nabla f \cdot \nabla f(\mathbf{x},t)$ associated with the "energy" $^1/_2 f^2(\mathbf{x},t)$ in the original field. This integral is then repeated as the effective resolution in the original measured data $f(\mathbf{x},t)$ is intentionally degraded by successively larger averaging windows. If the

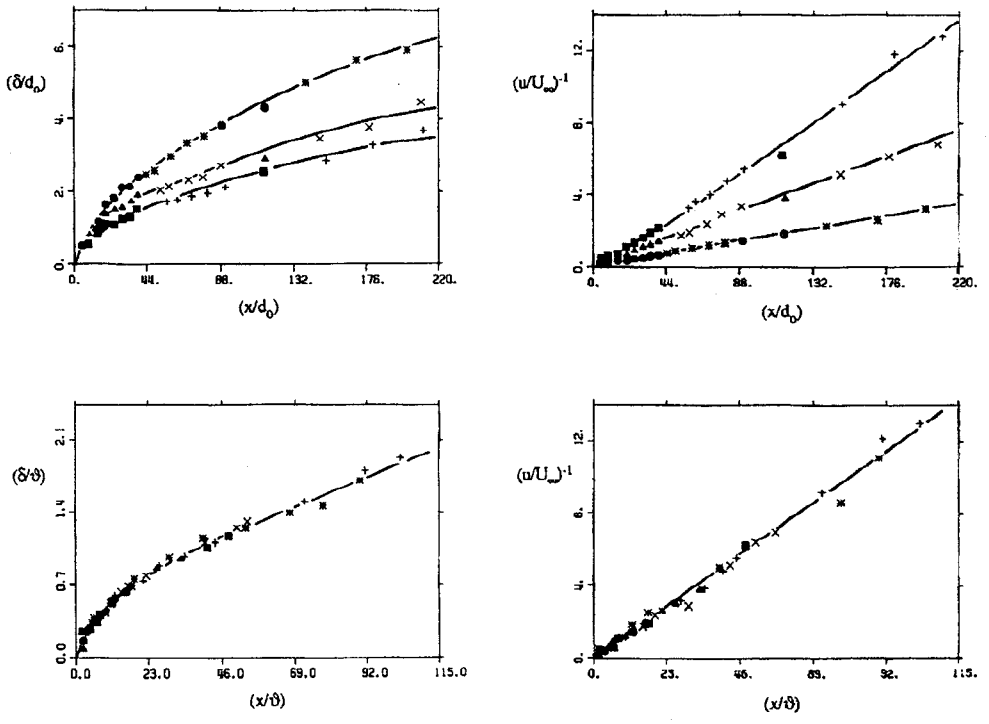

Figure 5. Outer flow scalings laws for axisymmetric coflowing turbulent jets, showing the variation in local flow width d and mean centerline velocity u with downstream distance x in simple jet variables *(top row)*, and in proper momentum variables *(bottom row)* giving the scaling functions $f_1(x/\vartheta)$ and $f_2(x/\vartheta)$. These determine the local outer-scale Reynolds number Re_δ and the local inner scale λ_v, which determines the spatial resolution requirements for the measurement.

resulting total dissipation approaches a resolution-independent value, then the data are fully-resolved. Such a procedure has been used by Southerland & Dahm (1996) (see also Dahm & Southerland 1999) to verify full resolution in turbulent flow measurements.

5. Coflowing Turbulent Jet Facility

The present measurements are obtained on the inner scales of an axisymmetric coflowing turbulent jet at local outer-scale Reynolds number $Re_\delta \approx 6{,}000$. However, as noted in §4, owing to the fact that Re_δ is sufficiently high and the measurements span a range of scales that is sufficiently small in comparison with the local outer length scale δ, the results from this study will be indicative of the universal structure and dynamics of all high Reynolds number turbulent flows. The particular choice of a coflowing turbulent jet as the flow field is not directly relevant to the results, and is instead purely a matter of experimental convenience, since this readily allows for seeding uniformity and elimination of seed from the test facility.

Coflowing Turbulent Jet Scaling

The downstream location x at which the measurements are conducted determines the local outer variables δ and u, which in turn dictate the local inner length scale λ_v and the advection time scale T_v that must be resolved by the measurements. The outer variables in axisymmetric coflowing turbulent jets follow non-algebraic far field similarity scalings first noted by Maczynski (1962). Letting U_∞ denote the coflow velocity in the free stream, these scalings can be easily understood by recognizing that when $(u/U_\infty) \to \infty$, the effect of the coflow should become locally negligible and the flow should approach the scaling for an axisymmetric turbulent jet issuing into a quiescent medium, for which

$$\delta \sim x \qquad u \sim \left(J_0 / \rho_\infty\right)^{1/2} x^{-1} \tag{4}$$

where J_0 is the jet source momentum flux and ρ_∞ is the ambient fluid density. In the opposite limit, when $(u/U_\infty) \to 0$, the momentum flux integral in terms of the excess velocity $u \equiv (U - U_\infty)$ becomes identical to that obtained for a wake in terms of the deficit velocity. In that case, self-similarity requires the simple algebraic scalings

$$(\delta / \vartheta) \sim (x / \vartheta)^{1/3} \qquad (u / U_\infty) \sim (x / \vartheta)^{-2/3} \tag{5}$$

where ϑ denotes the invariant momentum radius of the flow, given by

$$\vartheta^2 \equiv \frac{J_0}{\pi \rho_\infty U_\infty^2} \quad . \tag{6}$$

Note that, in terms of the proper dimensionless downstream similarity coordinate (x/ϑ), the wake-like limit in (5) corresponds to $(x/\vartheta) \to \infty$. At the other extreme, the jet-like limit in (4) corresponds to $(x/\vartheta) \to 0$, and can be equivalently written in terms of ϑ as

$$(\delta / \vartheta) \sim (x / \vartheta) \qquad (u / U_\infty) \sim (x / \vartheta)^{-1} \tag{7}$$

Equations (5) and (7) suggest that, over the entire range $0 < (x/\vartheta) < \infty$, the axisymmetric coflowing turbulent jet will follow

a non-algebraic similarity scaling of the form

$$(\delta / \vartheta) \sim f_1(x / \vartheta) \qquad (u / U_\infty)^{-1} \sim f_2(x / \vartheta) \qquad (8)$$

with the scaling functions f_1 and f_2 satisfying the asymptotic power-law limits noted above. Measurements by Reichardt (1965) and Biringen (1975), and more recently by Nickles & Perry (1999), have confirmed these similarity scalings and give the scaling functions f_1 and f_2 as shown in Fig. 5.

Coflowing Jet Facility

The axisymmetric coflowing turbulent jet used in this study is formed by issuing air through a central tube with 2.2 mm inner diameter surrounded by a square (305 mm × 305 mm) duct containing a coflow of air. The arrangement of the facility is shown in Fig. 6. The central tube runs from the base of the facility through a flow conditioning section to the exit plane of the test section. The exit of the tube is slightly tapered. The coflow is formed by the induced draft from a fan far downstream of the test section, and enters the test section through five large holes in the bottom of the facility. These holes provide for a highly turbulent flow in a seeding section, in which PIV seed injected through the side walls and mixes with the induced coflow air to produce an essentially uniform particle seeding density. The coflow then proceeds through a flow management section consisting of an appropriate arrangement of a porous plate, mesh screens, and a honeycomb. This design of this section was based on empirical guidelines to provide a uniform coflow with reasonably low turbulence intensity. Standard PIV and stereo PIV measurements verified an essentially uniform 0.25 m/s coflow velocity throughout the test section with less than 6% turbulence intensity. A glass duct extends the coflow through the test section and kept drafts from disturbing the flow field. An exhaust hood located 2.0 m downstream of the jet exit removes the PIV seed from the containment. The seeding density is adjusted to provide a high percentage of good vectors in the DSPIV data. Both the central jet and the coflow are seeded to avoid any biasing and areas of low seed density due to velocity gradients and fluid entrainment.

All measurements are made on the jet axis 100 diameters downstream of the jet exit (x = 22 cm), where the local mean centerline velocity $u \approx 0.98$ m/s and the local jet width $\delta \approx 9.6$ cm. These values are obtained from the scaling laws in (8) for the $U_\infty = 0.25$ m/s coflow velocity and the jet momentum flux J_0 implied by the jet flow rate (measured by a laminar flow element) and the assumed fully-developed pipe flow velocity profile. Note that the experiments are conducted at a sufficiently small (x/ϑ) value to be in the noncoflowing limit (*i.e.*, in the jet-like limit), for which the coflowing free stream serves only to provide a uniform source for PIV seed to be entrained into the turbulent jet.

The measurement location in the jet far-field is selected based on a trade-off between the imaging requirements of the DSPIV system and the local inner length scale associated with the turbulent flow. For these experimental conditions, the local outer-scale Reynolds number $Re_\delta \approx 6{,}000$, which in turn produces a local inner (viscous) length scale $\lambda_\nu \approx 1600$ μm. This inner length scale and the $\Delta \approx 400$ μm effective spatial resolution of the present DSPIV imaging configuration in §2 determines the relative resolution achieved by the measurements. Following the results

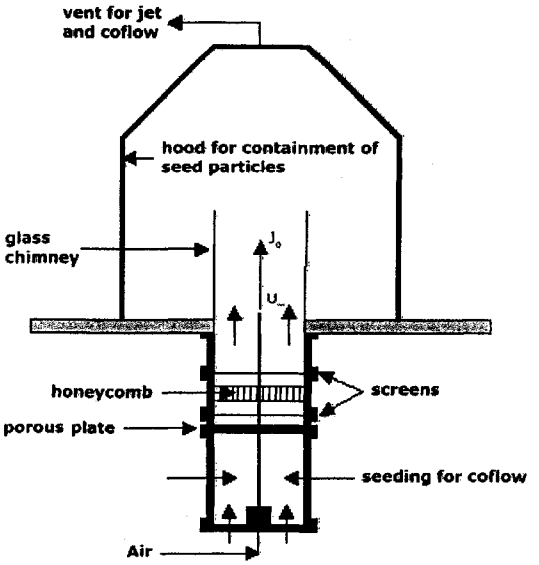

Figure 6. Schematic indicating layout of coflowing turbulent jet facility used in the present study, showing seeding section, flow management section, test section, and containment hood.

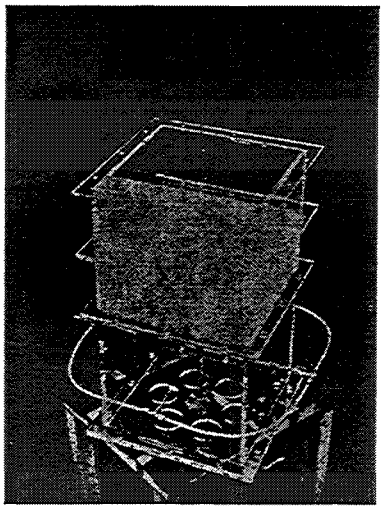

Figure 7. Photograph of the seeding and flow management sections, showing the central tube and the air induction holes.

CCD Sensor Format	1280 × 1024
Pixel Size	6.7 μm
Camera Magnification Factor	1.82
Interrogation Window Size	32 pixels
Effective Spatial Resolution	400 μm
Local Mean Velocity u	0.98 m/s
Local Flow Width δ	9.6 cm
Reynolds Number Re_δ	6,000
Inner Length Scale λ_ν	1600 μm

Table 1. Imaging parameters, local outer-scale parameters, and local inner-scale parameters relevant to the spatial resolution of the present DSPIV measurements.

of Southerland & Dahm (1996) and Dahm & Southerland (1999) for the "grid convergence" procedure in §4, with $(\lambda_v/\Delta) \approx 4$ the present measurements should resolve approximately 90% of the total dissipation associated with the turbulent velocity field.

6. DSPIV Implementation Issues

Light Sheet Characterization

A central matter in any DSPIV measurement is the thickness, spacing, and parallelism of the two differentially-separated light sheets, which directly contribute to the accuracy achievable by the measurements. If not accounted for, these imperfections will be manifested in the calibration and mapping of the cameras and therefore in the velocity derivatives that result from the DSPIV measurements. This section therefore gives a discussion of the source of these errors and how they can be controlled. A discussion of how the remaining errors can be accounted for is given in the calibration error analysis section.

The light sheet thickness is one of the components of the spatial resolution involved in the measurement. In the present study, the sheet thickness is measured in the center of the measurement region by traversing a small pinhole across the sheet and collecting the transmitted light onto a photodiode detector. To quantify the sheet thickness, a gaussian fit is determined for the resulting measured intensity profile by calculating the three lowest order moments of the measured intensity profile and matching these to the corresponding three moments of a gaussian function. This allows for the centerline position, the local intensity maximum, and the local $1/e^2$ width of the laser sheet to be determined. Typical results are shown in Fig. 8*a*. It is apparent that the intensity profiles across the green and red light sheets are only roughly gaussian, but that the resulting thickness measures nevertheless provide a reasonable characterization of their thickness. The variation in thickness along the vertical extent of the light sheet is obtained from analysis of sheet images, with typical results in Fig. 8*b* verifying that the sheet thickness is essentially uniform.

The separation between the green and red light sheets is crucial for the mapping between the two SPIV measurement planes, and in calculating the central differences used to determine the velocity gradients. Errors in the separation distance, or changes in this distance due to nonparallelism of the sheets, will directly effect the accuracy of the derivatives in the out-of-plane direction. The procedure for separating the light sheets begins with the two light sheets initially coincident. The red sheet is then moved, by rotation of a mirror, in the z-direction to create the necessary separation. The two light sheets are blocked by a semi-transparent target to create an image of the sheet cross sections with one of the cameras. Two double frame/double exposure images are taken for the analysis. The first image captures the 532nm sheets and the second captures the 635nm sheets. The camera is not moved and the lasers are positioned to obtain these images in the same field-of-view. From these images, intensity profiles are obtained by averaging every 16 rows, and a gaussian fit is made using the same procedure as noted above. From this gaussian fit, the center location of the intensity profile is obtained for each of the four laser sheets. Figure 9*a* shows how the respective laser sheet central points vary along the vertical direction, and verifies that each color-pair of light sheets is virtually coincident (in comparison with the sheet thickness) and that the spacing between the green and red sheets is constant over the vertical extent of the light sheets.

The four light sheets must also remain parallel over the entire field-of-view of the PIV cameras. This parallelism is assessed by conducting the procedure described above at the left and right edges of the field-of-view, in addition to the center of the field-of-view. The separation between pairs of sheets should vary little if the sheets are essentially parallel. Figure 9*b* verifies that, for the optical configuration used here, the angle between the

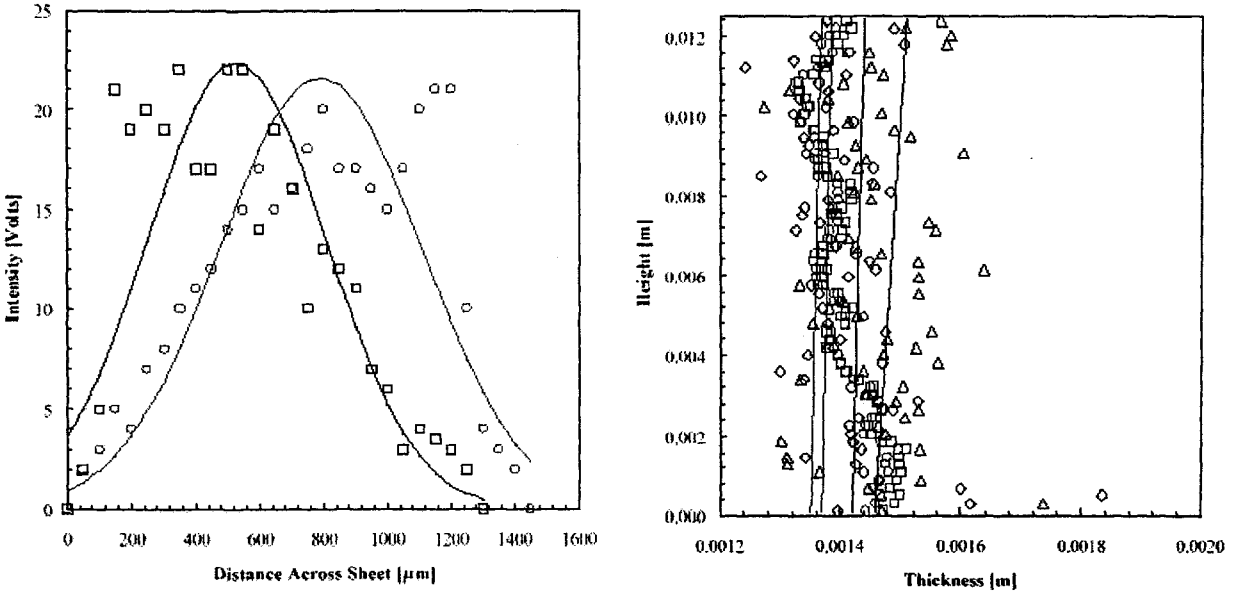

Figure 8. Results obtained from characterization of green and red laser sheet intensity profiles *(left)* measured with a traversing pinhole and photodiode and fit with a gaussian to determine $1/e^2$ thickness, and variation in thickness along vertical direction *(right)* from image analysis, showing that sheet thickness remains near constant.

green and red sheets is slightly less than 1-degree. Over the field-of-view, this produces a negligible variation in the sheet separation.

DSPIV Calibration

The accuracy of the velocity fields in any PIV method depends on accuracy of the particle measurements and the accuracy of relating the particle images to the respective particle displacements. These two issues are both related to the focusing of the cameras and the image distortion that is inherent in the stereoscopic imaging configuration. The issue of focusing is related to the particle image size, with the requirement being that the particle images should typically span 2-3 pixels on the CCD array. As the particle images become larger than this, the displacement of their centroids becomes increasingly difficult to measure accurately. The image distortion inherent in stereoscopic imaging is a result of variable magnification M across the image plane due to the off-axis viewing angle of the cameras. Because of this variable magnification, the simple relation between particle displacements (X_1, X_2) in the object plane and their displacements (x_1, x_2) in the image plane, namely

$$(X_1, X_2) = -M(x_1, x_2) \quad , \tag{9}$$

is no longer valid, but now takes on the form

$$\mathbf{X} = F(\mathbf{x}) \tag{10}$$

where F is a nonlinear mapping function created from a calibration procedure. These mapping functions correct the two-dimensional velocity fields to account for the distortion effects, and also provide the necessary information to calculate the third velocity component from the apparent in-plane components. The SPIV calibration method of Soloff, Adrian, & Liu (1997) is implemented here to calculate these mapping functions for the four cameras in the present DSPIV system. This general procedure eliminates the need to physically register each camera, and allows for a mathematical registration that greatly simplifies registering the four cameras.

The calibration is carried out using a calibration target consisting of a regular grid of crosses; images of the target from two of the PIV cameras are shown in Fig. 10. The spacing between the crosses and the thickness of the lines that constitute the crosses need to be accurately known. The required accuracy of the target, the forward-forward configuration of the DSPIV cameras, and the relatively small field-of-view needed for these measurements requires a transparent target approximately 2 cm × 2 cm in size. A full-size target was printed and then transferred to a 35 mm film negative with a known magnification. The distance between the crosses on the negative was verified under a microscope to be 660 μm. Since velocity vectors are only calculated in the overlapped regions of the four cameras careful alignment of the cameras is crucial. This was accomplished with micrometer translation stages mounted on traverses coupled with the calibration target. As seen in Fig. 10, a reference point is placed on the target that serves to define the origin for all the images. From the four target images, the camera magnification factors and their positions can be compared, and the necessary adjustments made to allow precise overlap of their respective fields-of-view. This also requires good focus across the target; small lens aperture settings are used along with the Scheimpflug condition to obtain the necessary focus across the image.

The calibration procedure described above consists of two independent stereoscopic PIV calibrations. In a DSPIV system, a further mapping is required to relate vectors from one stereo system to the other. Figure 11 shows the positions of the calibration target within the respective laser sheets for this DSPIV calibration. Since it is the relative positions of the target that are important and not the absolute location within each light sheet, the target locations are chosen to be the front and back faces of the laser sheets respectively. This implies the target only has to be

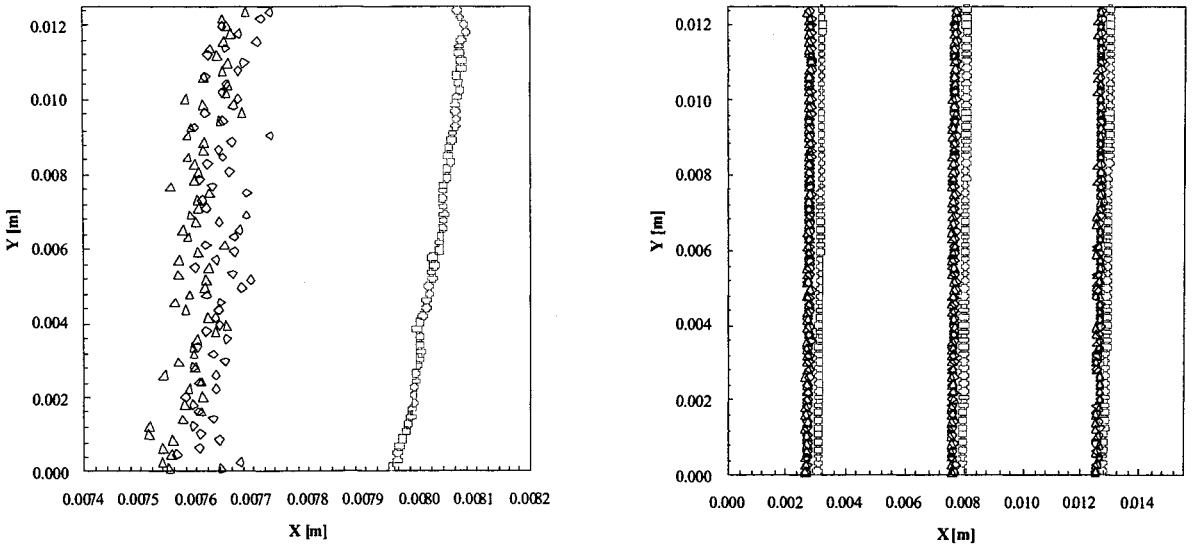

Figure 9. Results from characterization of laser sheet parallelism, showing measured variation in spacing between centers of green and red sheets along vertical direction near middle of field-of-view *(left)*, and variation in measured spacing along vertical direction at the three different locations spanning across full field-of-view, verifying that sheets are essentially parallel.

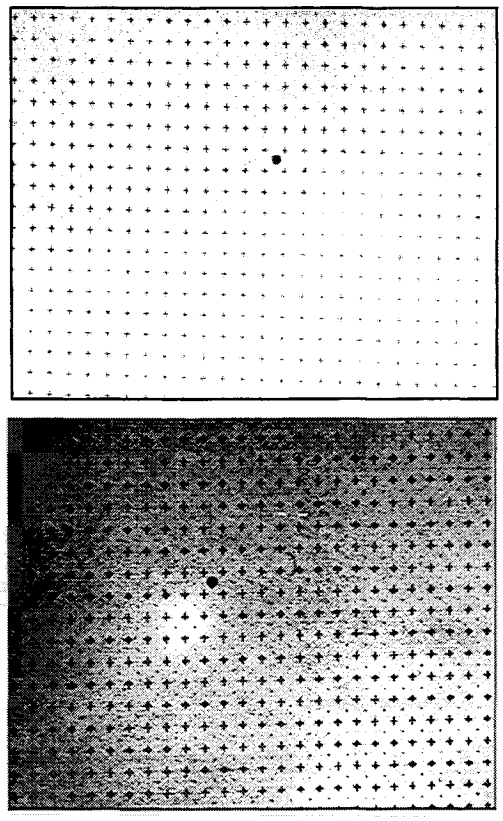

Figure 10. Images from one camera pair of the high-resolution calibration target on 35 mm film negative, showing reference point and crosses used to obtain mapping function in (10).

Figure 11. Diagram showing calibration target locations for each of cameras 1 and 2 in green sheet, and cameras 3 and 4 in red sheet.

displaced twice, with the middle target location serving as both the displaced plane for the green light sheet and the initial plane for the red light sheet. The calibration is carried out by taking the first two images for the green cameras and then displacing the calibration target by a known distance with the micrometer translation stage. The second two images are then obtained and the mapping functions generated. The mapping functions are created by first locating the positions of the crosses with respect to the image origin in each respective image, using a centroid identification algorithm. Once these origins are defined, a two-dimensional 3rd-order polynomial is generated using a least squares error minimization technique to create the in-plane mapping function for each camera. To construct the mapping for the out-of-plane component, the difference in z-direction mapping between the planes is used. The registration of the cameras is done automatically within the mapping using the defined origin and the calculated physical size of each image. Once the first SPIV system is calibrated, the second calibration is carried out in the same manner, the only difference being the automatic registering of the cameras to each other and to the cameras from the first sheet. This calibration procedure results in four mapping functions of the type in (10), which are subsequently used to obtain the three velocity vector components (u, v, w) across the field-of-view from the particle displacement images.

Error Analysis for the Calibration Procedure

Since the DSPIV system calibration described above generates the mapping functions in (10) that relate the particle displacements to the velocity vectors, any errors accrued in these calibrations will affect the accuracy of the resulting velocity fields. It is thus essential to understand the error sources that can arise in this calibration process. There are five possible sources of error in the procedure described above: *(i)* errors in the cross spacing on calibration target, *(ii)* errors introduced by approximating the true mapping function with a 3rd-order polynomial, *(iii)* errors introduced by imperfect parallelism of the calibration planes relative to each other, *(iv)* errors due to the calibration planes not being precisely parallel to light sheets, and *(v)* errors introduced by the absolute positions of the calibration planes within each light sheet. Each of these will be discussed in turn, with the associated error estimates applicable for the present measurements being assessed.

Inaccuracy in measurement of the cross spacing on the calibration target introduces an error in the mapping function, however since both the cross separation on the original large-scale printed target and the magnification factor used to reduce this to the 35 mm film negative is accurately known, the resulting uncertainty in the cross separation on the target is only about 10 μm. This is completely negligible in comparison with other error sources. The second error source is due to the true mapping function being approximated by simple 3rd-order polynomial, however from prior results with SPIV systems this is know to provide accurate results for camera angles up to 45-degrees. For the DSPIV arrangement used here, camera angles are 20-degrees and 30-degrees (see Fig. 4), and thus the resulting errors should be very small. The third error source is due to the calibration target planes not being exactly parallel to each other. However the calibration procedure uses a 3/8" Plexiglas mount to hold the target, with the mount being moved by a micrometer stage having 1μm accuracy. This would suggest that any nonparallelism in the target planes should be significantly smaller than 1μm. The fourth error source comes from the requirement that the calibration target should be precisely parallel to the light sheets. If the calibration target plane is at some angle with respect to the light sheet plane, then the mapping functions are appropriate for the velocity field in the rotated coordinate system and not the coordinate system of the light sheet. This appears to be the greatest source of error in the calibration procedure. The final error source is due to the absolute location of the calibration target within the light sheets, however since the velocity vectors obtained from the PIV measurements are implicitly averaged over the thickness of the light sheet (and the correlation window size). The calculated vectors are averaged over the thickness of the light sheet and the thickness of the light sheet is small compared to the distance between the sheet and the camera. The relative error of the calibration target location is then small compared to the distance of the camera.

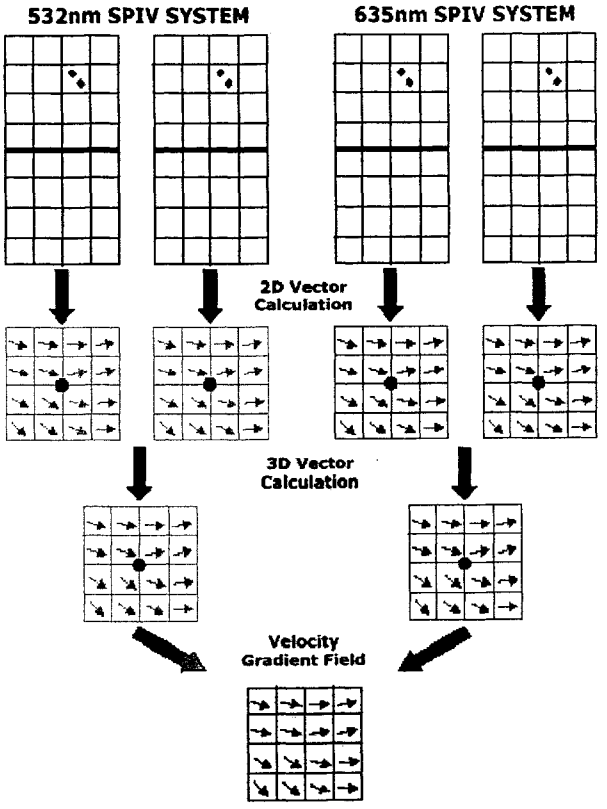

Figure 12. Schematic indicating process by which raw particle image pairs on each of the four PIV cameras are used to obtain the velocity gradient tensor field.

Vector Calculation Using the Mapping Function

Once the DSPIV system calibration is complete and the mapping functions have been created, the velocity fields can be obtained from the particle image pairs. The eight particle images from the DSPIV system are transferred from the cameras in the double frame/double image format and stored on the computer in a single file. Four two-dimensional vector files are obtained, two for each set of cameras, with their size corresponding to the overlapped region of the mapping functions for the respective cameras. For each position in the vector file, the corresponding location of the interrogation window in the particle image is analyzed. These four two-dimensional vector files are then used to create the final two three-dimensional vector files using the mapping functions to correct for the distortion and to calculate the out-of-plane component of the velocity. Figure 12 illustrates this process. The out-of-plane component of each vector is calculated from the respective components of the two two-dimensional vectors at the same location and the transformations defined in the mapping function. This is an over-determined system, allowing for a check on the computed vectors. One component of velocity is thus calculated twice and compared to ensure that the difference is below a threshold value. Once this validation has been done, the resulting green and red three-component vector planes are complete and can be used with central difference operators to create the velocity gradient quantities of interest.

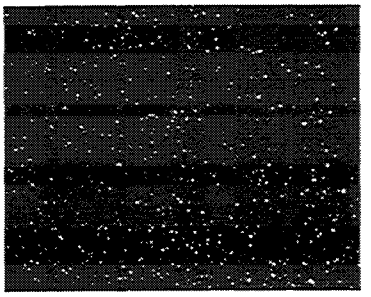

Figure 13. Synthetic particle image used for DSPIV system performance characterization.

Resolution

The resolution limits introduced by the measurement process and the subsequent data processing are of key importance, since this study aims to use these velocity measurements to obtain velocity gradient quantities. This section addresses the implicit filtering of the velocity fields inherent in the PIV processing. The various PIV processing operations effectively act as filtering processes on the true velocity field. There are five principle factors that contribute to the resolution of the PIV measurements: the laser sheet thickness, the PIV correlation window size, the typical bad-vector replacement region size, the PIV processing filter scale, and the spectrally-sharp derivative filter scale. As discussed in §2, the laser sheet thicknesses are 800 μm for both sheets. The 32 × 32 pixel PIV correlation window, together with the pixel size and magnification ratio, effectively filters the velocity field at a scale of approximately 400 μm. The explicit filtering done as part of the PIV processing is at a scale of 400 μm. Based on the spacing of the vectors, the bad vector replacement regions are 400 μm. Lastly, the velocity gradient fields $\nabla\mathbf{u}(\mathbf{x},t)$ produced by the resulting vectors are processed with a spectrally-sharp filter at a scale of 800 μm. Since these contributions to the net PIV resolution are essentially independent, the resulting velocity gradient fields are thus resolved to a length scale of $\lambda_{net} \approx 1325\ \mu$m. This effective resolution of the DSPIV system, for the current configuration, must be compared with the local inner scale $\lambda_v \approx 1600\ m$m. Based on these scales, the measured values of any arbitrary velocity gradient quantity $q(\mathbf{x},t)$ can be related to the actual values as

$$\frac{\tilde{q}(\mathbf{x},t)}{q(\mathbf{x},t)} \approx \left[1+\left(\frac{\lambda_{net}}{\lambda_v}\right)^2\right]^{-1/2}. \qquad (11)$$

From (11) and the given values above, the measured gradient quantities are about 0.59 times the true values. Future improvements to this system will enhance the net resolution scale.

7. DSPIV System Performance

Prior to conducting actual measurements with this DSPIV system, the theoretical system performance was studied. The accuracy of the velocity measurements and the uncertainty introduced in the calibration procedure must be checked to establish a baseline performance level for the system. Lawson & Wu (1997) and Coudert *et al* (1999) have performed theoretical and experimental studies of the symmetric and asymmetric camera positions for the stereoscopic PIV arrangement. For the present con-

	δ_{ave}	δ_{err}	δ_{rms}
δx	380 μm	5.0%	0.010
δy	410 μm	2.5%	0.011
δz	420 μm	5.0%	0.060

Table 2. Measured displacements obtained from synthetic particle images displaced by 400 μm in each direction, and the associated mean and rms errors.

figuration, error ratios based on these studies should be no greater than 3 to 4. To check this, synthetic particle images of the type shown in Fig. 13 were mounted on an x-y-z micrometer traverse and used to create the known displacements. The images were displaced 400 μm in each direction and the system acquired images at the various displaced locations, allowing for the measured displacements to be compared to the true displacements. Table 2 shows the averaged measured displacements for the image and the rms errors associated with them.

The error ratio as defined by Lawson & Wu (1997) is

$$er \equiv \frac{\delta z_{rms}}{\delta x_{rms}} \tag{12}$$

with δz_{rms} is the out-of-plane rms error and δx_{rms} is the in-plane rms error. Based on the results in Table 2, for the present DSPIV system this error ratio is 2, which agrees well with the findings of Lawson and Wu and Coudert *et al* (1999).

8. Preliminary Results

Figure 14 presents three-component velocity fields measured in the green and red light sheet planes using the present DSPIV system. The system configuration is as described above, with 800 μm laser sheet thicknesses and 400 μm sheet separation. The velocity fields were obtained on the centerline of the axisymmetric coflowing turbulent jet at $Re_\delta \approx 6{,}000$. The field-of-view shown in Fig. 14 spans approximately 9.7 $\lambda_\nu \times 7.8\ \lambda_\nu$, and thus the velocities on these comparatively small length scales should be essentially independent of both the particular turbulent flow and the particular Re_δ value at which they were obtained. It is apparent from the velocity vectors in the two planes in Fig. 14*b* that the same flow structures are being resolved in both planes. This is consistent with the small spacing between these planes, which is shown at greatly exaggerated scale in the figure. While these results are preliminary, they indicate the potential of such measurements for revealing the small scale structure of turbulent flows at conditions that are well beyond the reach of direct numerical simulations.

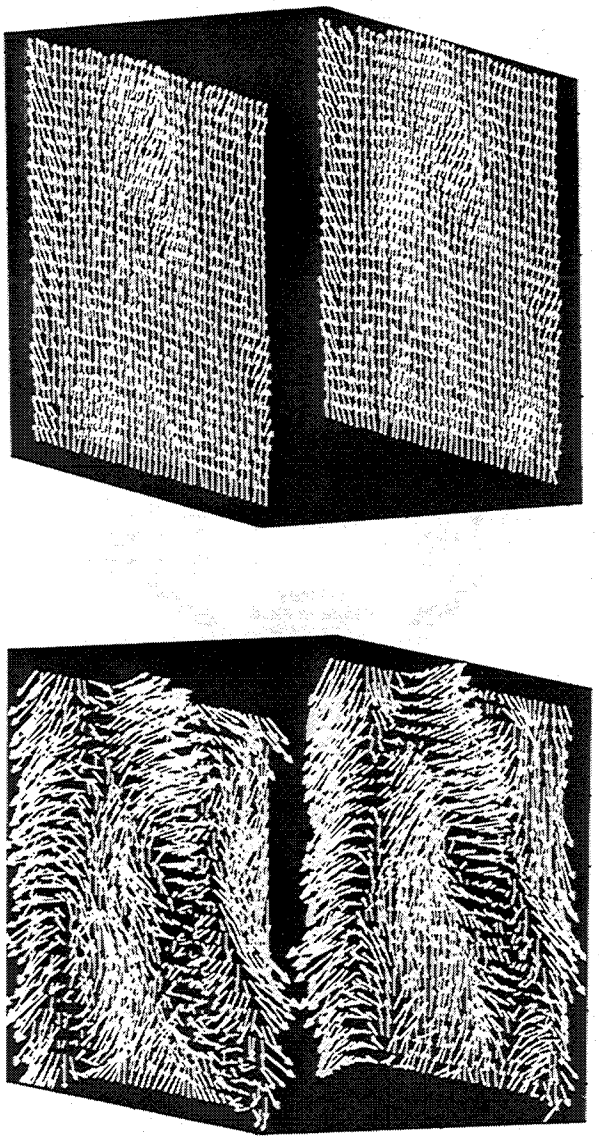

Figure 14. Preliminary three-component velocity vectors in the green *(left)* and red *(right)* planes from the present DSPIV measurements. Sheet separation is shown greatly exaggerated for clarity. Shown are the absolute velocities *(top)* and the velocities with the mean flow subtracted *(bottom)*.

9. Conclusions

This paper has summarized the frequency-based approach to dual-plane stereoscopic PIV for velocity field measurements in turbulent flows, and has presented preliminary velocity vector field measurements with such a system. These allow direct experimental access to the structure and dynamics of the full velocity gradient tensor at the quasi-universal small scales of turbulent flows. Several key issues of the measurement technique were described in detail namely:

1. Spatial scales and spatial resolution issues that determine whether any PIV technique can fully capture the structure of the flow at the scales measured.

2. A description of the forward-forward scattering configuration that optimizes the scattering intensity. The included angle was held constant, implying an asymmetric arrangement of the

respective camera pairs. This configuration resulted in accurate measurement of the displacement field, as confirmed by the synthetic PIV results.

3. The laser sheet thickness, separation, and parallelism are central to this measurement technique. Methods for quantitatively assessing these issues were developed and the results implemented in the calibration, measurement, and post processing of the velocity fields.

4. The preliminary velocity fields in Fig. 14 showed encouraging agreement of the velocity fields in the two differentially-spaced planes, indicating that the data are differentiable. Future work is necessary to improve the agreement on a vector to vector basis and furthering the data reduction to gain access to the dynamical quantities such as the vorticity field, enstrophy field, and kinetic energy dissipation field.

Acknowledgements

Part of the work presented here has been supported by the Air Force Office of Scientific Research under AFOSR Grant No. F49620-95-1-0115. The technical assistance of Dr. Callum Gray and Uwe Dierksheide of LaVision, GmbH is gratefully acknowledged, as is assistance by Prof. N. Ninomiya on a sabbatical leave from Utsonomiya University.

References

Hu, H., Sata, T., Kobayashi, T., Taniguchi, N. & Yasuki, M. (2001) Dual-plane stereoscopic particle image velocimetry: system set-up and its application on a lobed jet mixing flow. *Expts. Fluids* **31**, 277-293.

Coudert, S., Westerweel, J. & Fournel, T. (1999) Comparison between asymmetric and symmetric stereoscopic DPIV system. Proc. 10th Annual Symp. on Laser Techniques Applied to Fluid Mechanics., Lisbon, Portugal.

Dahm, W.J.A. & Southerland, K.B. (1999) Quantitative flow visualization via fully-resolved four-dimensional spatio-temporal imaging. Chapter 11 in Flow Visualization: Techniques and Examples, (A. Smits and T.T. Lim, Eds.), 231 - 258, Imperial College Press, London.

Lawson, N.J. & Wu, J. (1997) Three-dimensional particle image velocimetry: experimental error analysis of a digital angular stereoscopic system. *Meas. Sci. Technol.* **8**, 1445-1464.

Prasad, A.K. & Jensen, K. (1995) Scheimpflug stereocamera for particle image velocimetry in liquid flows. *Appl. Optics*, 34, 7092-7099.

Willert, C. (1997) Stereoscopic digital particle image velocimetry for application in wind tunnel flows. *Meas. Sci. Technol.* **8**, 1465-1479.

Virant, M. & Dracos, T. (1997) 3D PTV and its application on Lagrangian motion. *Meas. Sci. Technol.* **8**, 1539-1552.

Bruckner, C. (1997) 3D scanning PIV applied to an airflow in a motored engine using digital high speed video. *Meas. Sci. Technol.* **8**, 1480-1492.

Meng, H. (1999) Tackling turbulence with holographic particle image velocimetry (HPIV). *AIAA Paper No.* 99-3755, 30th AIAA Fluid Dynamics Conference, AIAA, Washington D.C.

Raffel, M., Gharib, M., Ronneberfer, O. & Kompenhans, J. (1995) Feasibility study of three-dimensional PIV by correlating images of particles within parallel light sheet planes. *Exp. Fluids* **19**, 69-77.

Kahler, C.J. & Kompenhans, J. (1999) Multiple plane stereo PIV: technical realization and fluid-mechanical significance. *Proc. 3rd International Workshop on PIV*, Santa Barbara, U.S.A.

Soloff, S.M., Adrian, R.J. & Liu, Z.C. (1997) Distortion compensation for generalized stereoscopic particle image velocimetry. *Meas. Sci. Technol.* **8**, 1441-1454.

Southerland, K.B. & Dahm, W.J.A. (1997) Experimental assessment of Taylor's hypothesis and its applicability to dissipation estimates in turbulent flows. *Phys. Fluids* **9**, 2101-2107.

Su, L.K. & Clemens, N.T. (1998) The structure of the three-dimensional scalar gradient in gas-phase planar turbulent jets. *AIAA Paper No.* 98-0429, 36th AIAA Aerospace Scioences Meeting, AIAA, Washington D.C.

Su, L.K. & Clemens, N.T. (1999) Three-dimensional measurements of fine-scale mixing in gas-phase planar turbulent jets. *Proceedings of FEDSM99*, ASME/JSME Fluids Engineering Summer Meeting, ASME.

Su, L.K. & Clemens, N.T. (1999) Planar measurements of the full three-dimensional scalar dissipation rate in gas-phase turbulent flows. *Expts. Fluids* **27**, 507-521.

Raffel, M., Willert, C. & Kompenhans, J. (1998) Particle Image Velocimetry: A Practicle Guide, Springer, New York.

Samimy, M. & Lele, S.K. (1991) Motion of particles with inertia in a compressible free shear layer. *Phys. Fluids A* **3**, 1915-1923.

Southerland, K.B. & Dahm, W.J.A. (1996) Fully-resolved four-dimensional measurements of the small-scale structure of passive scalar mixing in turbulent flows. *Report No. 026779-12*, The University of Michigan, Ann Arbor.

Melling, A (1997) Tracer particles and seeding for particle image velocimetry. *Meas. Sci. Technol.* **8**, 1406-1416.